Enhanced photocatalytic degradation of methylene blue: Preparation of TiO₂/reduced graphene oxide nanocomposites by direct sol-gel and hydrothermal methods

Hicham Atout[a], Mayra G. Álvarez[b,c], Derradji Chebli[a], Abdallah Bouguettoucha[a], Didier Tichit[c], Jordi Llorca[d], Francesc Medina[b]

[a]Département de Génie des Procédés, Laboratoire de Génie des Procédés Chimiques, Faculté de Technologie, Université Ferhat Abbas, Sétif-1, 19000 Sétif, Algérie Email: attoutishak@gmail.com; abdallah.bouguettoucha@univ-setif.dz; derradji.chebli@yahoo.fr

[b]Department of Chemical Engineering, University Rovira i Virgili, 43007 Tarragona, Spain E- mail : francesc.medina@urv.cat [c]Institute Charles Gerhardt, Equipe Matériaux Avancés pour la Catalyse et la Santé, 34296
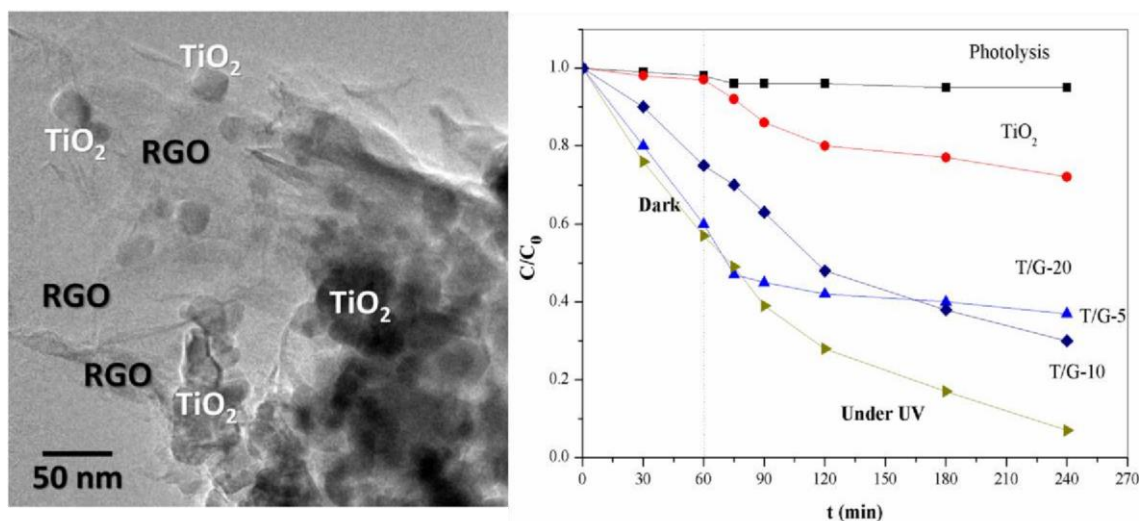
Montpellier Cedex 5, France

E- mail : mayra.garcia@urv.cat , E- mail : tichit@cit.enscm.fr [d]Institute of Energy Technologies and Centre for Research in Nanoengineering, Technical

University of Catalonia, 08028 Barcelona, Spain

E- mail : jordi.llorca@upc.edu

Graphical abstract

Highlights

- TiO₂-RGO nanocomposites presented, in all the cases studied, improved photocatalytic properties compared to bare TiO_2.

- An optimal composition, in terms of TiO_2/RGO ratio was found in both series of nanocomposites; however, superior activity was found for those prepared by direct sol-gel route.

- Nanocomposites prepared by sol-gel method presented improved textural properties than those prepared following a hydrothermal route.

- Optimization in the preparation of hybrid photocatalystsis needed to obtain materials with finer properties for effective application in environmental

Abstract

In this study, two different preparation methods of titanium dioxide nanoparticles/reduced graphene oxide nanocomposites were investigated using direct sol-gel method followed by

2

hydrothermal treatment or simple hydrothermal route. A different amount of graphene (1-20%) was mixed with TiO_2 for both series of samples in order to improve the photocatalytic activity. The influence of the preparation method on the physico-chemical properties was established by different characterization methods and the photocatalytic degradation of methylene blue (MB) under UV light irradiation was used as test reaction. The highest photocatalytic activity was observed for the nanocomposites containing 10 wt% of graphene. The elimination of MB can reach 93% and 82% for the nanocomposites with 10 wt% graphene prepared by the sol-gel and hydrothermal methods, respectively. These photocatalysts are promising for practical application in nanotechnology.

1. Introduction

Today's advances in nano-science and nanotechnology make possible the use of nanomaterials to develop more cost effective and environmentally acceptable water purification processes [1-6].

Among the different methods, photocatalysis is currently presented as a highly promising and efficient one. In this regard, TiO_2 is the most investigated material as photocatalyst due its well-known properties such as wide band gap semiconductor, high redox potential, cheapness, non-toxicity and chemical stability. Specially, TiO_2 has demonstrated activity for photocatalytic decontamination of waters containing (azo) dyes from textile and cosmetic industries [7-14]. However, due its low quantum yield and high recombination ability of photo-generated electron-hole pairs it is poorly efficient [15].

A common method for enhancing the photocatalytic efficiency of TiO_2 is to support it on a suitable matrix such as zeolites, silica [16,17] or carbon-based materials, including activated carbon and carbon nanotubes (CNTs) [18-21] and, as most recently performed, graphene or graphene oxide (GO) which has emerged as one of the most promising and technologically powerful materials, with multiple potential applications in several fields.

To the well-known properties of graphene (zero band gap semiconductor, high electron mobility [22,23], theoretical surface area (2630 m^2/g) and thermal conductivity), it should be added its surface tunability. The surface properties of graphene can indeed be adjusted by functionalization via chemical species (e.g. carboxyl, hydroxyl, epoxy among other organic groups), which makes graphene a very attractive building block for the preparation of composite materials. Thus, a proper combination of graphene and TiO_2 would give rise to nanocomposites exhibiting the properties of the respective building nanoscaled components with eventual synergetic effect allowing high efficiency for specific applications. A fairly large number of preparation methods of nanocomposites obtained from TiO_2 and graphene for photocatalytic applications have been reported which include thermal and solvothermal reactions, sol-gel route [24,25], hydrolysis, impregnation, liquid phase deposition [26-28]. Such nanocomposites are efficient photocatalysts for degradation of organic pollutants in water [20,29-33] due to the extended photo responding range, enhanced charge separation and transportation properties compared to either bare TiO_2 or other TiO_2containing composites. However, it is difficult to establish the influence of the preparation method of the materials since the results were obtained using different experimental setups (e.g., pH, light source, concentration, time, precursor material, solid/liquid ratio…).

In this study, we present the preparation of two series of TiO_2 and RGO-containing composites obtained either by simple hydrothermal route or direct sol-gel deposition where, GO content was varied (from 5% to 20%, (w/w)). We particularly studied the influence of the preparation method on the physico-chemical features of the corresponding nanocomposites

and on their photocatalytic activity. These prepared composites were indeed employed as photocatalysts to decolorize methylene blue (MB) solution under UV light irradiation. MB dye was selected as modal contaminant for the photo-degradation experiments due to its presence in industries and wastewaters. The influence of both, the preparation method and the RGO content on the photocatalytic activity for MB degradation is reported.

2. Experimental section

2.1. Materials

Nature flake graphite (carbon content: 99.8 %, -325 mesh) and $KMnO_4$ (98%) were purchased from Alfa Aesar. H_2O_2 (30%), H_2SO_4 (98%), $NaNO_3$ (analytical grade), HNO_3 (70%), titanium (IV) butoxide ($Ti(OC_4H_9)_4$, 97%) and methylene blue were purchased from SigmaAldrich and used without further purification. Deionized (DI) water was used throughout the experiments.

2.2. Preparation of the catalysts

2.2.1. Preparation of graphene oxide

Graphene oxide (GO) was synthesized from graphite powder by a slightly modified Hummer's method [34]. In a typical synthesis, 5 g of graphite powder and 2.5 g of $NaNO_3$ were added to 115 mL of concentrated H_2SO_4. The temperature of the mixture was kept below 20 °C by means of an ice bath and then 15 g of $KMnO_4$ was slowly added into the suspension. After 30 min, the temperature was increased to 35 °C and the mixture was kept for another 30 min after which 230 mL of DI water was added. Then, the temperature was increased to 90 ºC and the reaction was maintained for 1 h. The resulted suspension was further diluted with addition of 350 mL of H_2O and treated with 15 mL of 30 weight % (wt.%) H_2O_2 solution. The mixture was then cooled down to room temperature and repeatedly centrifuged and washed, first with a 5 wt.% HCl solution, second with H_2O until pH ≈ 5 and

finally with acetone to displace excess of water. The resulted solid was dried at 40 ℃ for 72 h.

2.2.2. Preparation of TiO$_2$ nanoparticles

TiO$_2$ nanoparticles were prepared by sol-gel method as reported elsewhere [35]. In brief, 20 g of titanium (IV) butoxide (Ti(OC$_4$H$_9$)$_4$) were first dissolved in 80 mL of ethanol at room temperature. Subsequently, 200 mL of a 0.025 M HNO$_3$ solution were added drop wise under vigorous stirring. The mixture was then stirred for 24 h at room temperature allowing hydrolysis of Ti(OC$_4$H$_9$)$_4$ to occur. The solid was then, separated and washed with deionized water and finally dried at 105 °C overnight. The dried solid was calcined at 500 °C under air for 3 h.

2.2.3. Preparation of T/G nanocomposites by sol-gel

T/G composites were prepared by a modified sol-gel method. First, the appropriate amount of GO was dispersed in deionized water with mechanical stirring for 1 h followed by ultrasonication for 1 h more. The pH of the dispersion was adjusted to 1.5 by addition of 0.025 M HNO$_3$. A second solution of 4.5 g of tetrabutyl titanate (Ti(OC$_4$H$_9$)$_4$) in 18 mL of ethanol was prepared and stirred for 1 h. Then, required amounts of GO dispersion were added drop wise to the Ti(OC$_4$H$_9$)$_4$ solution under ultrasonication. The different amounts of GO were calculated in the way that the final composites have a GO content of 5, 10 and 20 wt.%. The obtained solutions were transferred into a 100 mL Teflon-sealed autoclave and maintained at 120 °C for 5 h. Finally, the resulting products were filtered and washed with deionized water and ethanol, then dried at 60 °C for 15 h and thermally treated under flowing argon (50 mL·min^{-1}) at 500°C for 5h with a ramp of 2°C/min. The different composite materials were denoted as: T/G-5, T/G-10, and T/G-20.

2.2.4. Preparation of T/GS samples by hydrothermal route

T/GS composites with GO content (1, 5, 10 and 20 wt.%) were obtained via hydrothermal

method as reported elsewhere [36] with slight modifications. Briefly, different amounts of

GO were dispersed in deionized H_2O (50 mL) by mechanical stirring (1h) followed by

ultrasonication for 1 h, and then adjusted to ca. pH = 1.5 with a 0.025 M HNO_3 solution. Then

1 g of TiO_2 (prepared as abovementioned) was added to the obtained GO solution and stirred

for 2 h followed by 2 h of ultrasonication to get a homogeneous suspension. The suspension

was then placed in a 100 mL Teflon-sealed autoclave and maintained at 120 ℃ for 5 h to

simultaneously achieve the reduction of GO and the deposition of TiO_2 on the carbon

substrate. Finally, the resulting composite was recovered by filtration, rinsed with deionized

water and ethanol, and dried at 60 ℃ for 15 h. The resulting T/GS composites were thermally

treated under identical conditions than T/G composites. The different samples were denoted

as, T/GS-5, T/GS-10, and T/GS-20. RGO was prepared by the same method without adding

TiO_2.

3. Characterization

The textural properties of all the synthesized samples were measured by

N_2physisorption at -196 ℃ using a Quadrasorb SI surface analyzer. All the samples were

degassed in vacuum at 150 ℃ for 15 h prior to analysis. The specific surface area was

determined using the Brunauer-Emmet-Teller (BET) method from the range P/P$_0$ = 0.05-0.35

in the adsorption branch, while pore size distribution was calculated using the Barrett-Joyner-

Halenda (BJH) method applied to the desorption branch.

The crystallographic phases were characterized by X-ray diffraction with a Siemens D5000

diffractometer with a Bragg-Brentano-geometry and vertical 2-theta goniometer and operated

at 80 kV using Cu Kα radiation. Diffractograms were in a 2 theta range from 5° to 70° with an

angular step of 0.03° at 5 s per step. The samples were dispersed on a Si(510) low background sample holder.

Crystallite size and crystalline phase contents were calculated by means of the program TOPAS working under the programming mode (launch mode) with local routines. The crystallite sizes estimated for all phases were calculated using the integral breadth method. Using integral breadth instead of FWHM to calculate the crystallite size may reduce the effect of crystallite size distribution on the Scherrer constant K and therefore the crystallite size analysis is more accurate.

Thermogravimetric analysis (TGA) curves were recorded in a Perking Elmer Pyris STA 6000 apparatus. Typically, 5 mg of sample were dried *in situ* at 80 ºC for 30 min and then heated from room temperature to 900 ºC in 20 mL·min^{-1} of air, at a heating rate of 10 ºC/min. Raman spectra were recorded using T64000 Jobin Ivon spectrometer. Approximately, 10 mg of each sample was excited using an Ar laser operating at 514 nm and a power of 2 mW. TEM observations were performed on a JEOL JEM-2100 instrument at an accelerating voltage of 80 kV. HRTEM was performed at an accelerating voltage of 200 kV in a JEOL 2010F instrument equipped with a field emission source. The point-to-point resolution was 0.19 nm, and the resolution between lines was 0.14 nm. Samples were dispersed in alcohol in an ultrasonic bath, and a drop of supernatant suspension was poured onto a holey carboncoated grid. Images were not filtered or treated by means of digital processing, and they correspond to raw data.

The structural features of selected TiO$_2$-RGO nanocomposites were also studied with X-ray photoelectron spectroscopy (XPS) on a SPECS system equipped with an Al anode XR50 source operating at 150 mW and a Phoibos 150 MCD-9 detector. The pressure in the analysis chamber was always below 10^{-7} Pa. The area analyzed was approximately 2 mm × 2 mm. The pass energy of the hemispherical analyzer was set at 25 eV and the energy step was set at 0.1

eV. Data processing was performed with the Casa XPS program (Casa Software Ltd., UK). Binding energy (BE) values were centered using the C 1s peak at 284.8 eV. The atomic fractions (%) were calculated using peak areas normalized based on acquisition parameters after background subtraction, experimental sensitivity factors and transmission factors provided by the manufacturer.

Diffuse reflectance UV-VIS spectra (DRS UV-Vis) of pressed powder sample diluted with KBr were recorded on a Shimadzu (UV-3600 spectrophotometer with a Harrick Praying Mantis accessory) and determined by Kubelka-Munk while the band gap E (eV) was calculated by:

$$E = hc/\lambda \tag{1}$$

Where h is blank constant = 6.626 x 10^{-34} J·s, c: speed of light = $3·10^8$ m·s^{-1}, and λ: cut off wavelength (nm).

EDX was performed on the samples in ESEM using a FEI Quanta 600 microscope equipped with energy dispersive X-ray microanalysis from Oxford Instruments operating at high vacuum with an accelerating voltage of 20 kV and a working distance of 6.6 mm.

Photocatalytic tests

The photocatalytic tests were carried out at room temperature using a cylindrical shape reactor of 200 mL opened at the air equipped with an ultraviolet lamp with 365 nm and 24 W. The lamp was placed 20 mm beside the liquid surface. MB was chosen as the model molecule for the photodegradation experiments due to its huge presence in industries and wastewaters. In a typical procedure, 100 mg of catalyst were dispersed in 200 mL of MB solution with the starting concentration of 10 ppm at the natural pH of MB solution (pH = 6.2). Prior to UV irradiation, the suspension was stirred for 1 h in dark conditions, in order to establish the adsorption-desorption equilibrium. To follow the photocatalytic degradation of MB, 2 mL of suspension were withdrawn periodically and immediately filtered to separate the catalyst from

9

the solution and analyzed using UV-Vis spectrophotometer (Shimadzu, UV-1700) by measuring the absorbance at (664 nm). All the experiments were performed by triplicate.

2. Results and discussion

2.1. BET surface area

Nitrogen adsorption/desorption measurements were performed to determine the specific surface area of the prepared nanocomposites and the results were analyzed by BET method. The N_2 adsorption/desorption isotherms for all the prepared composites are shown in Fig.1 and textural data are given in Table 1.

The isotherm shapes of the different composites, as well as that of bare TiO_2 correspond to mesoporous materials, whereas RGO isotherm suggests the presence of both micro and mesoporosity (Fig. 1A). The BET surface area of T/G samples was significantly larger than that of the T/GS ones in the whole range of RGO contents. In addition, surface area, pore volume and average pore diameter go through a maximum value at GO content of 10 wt.% in T/G series (Fig 1B and 1C), whereas they increase continuously and then reach the maximum at 20 wt.% of GO loading for T/GS series. This is in agreement with the evolution of crystallite size found by PXRD in both series of samples. Besides, the average pore diameter is lower in both series of composites than in the bare TiO_2 component.

2.2. X-ray diffraction

The PXRD patterns of the prepared nanocomposites are shown in Fig. 2. All samples reveal peaks that can be assigned toTiO_2 in the anatase form in the case of T/G nanocomposites (Fig.2A). Whereas, small diffraction peaks at 2 theta angles 27.3°, 36.1° and 41.2°corresponding to planes (110), (101) and (111) respectively, indexed to rutile structure could also be observed in the case of T/GS composites(prepared by hydrothermal route), as well as in the bare TiO_2prepared by sol-gel method (Fig. 1B). These results suggest that rutile

phase formation is inhibited when TiO_2 is formed by sol-gel method in the presence of GO during the synthesis of the T/G nanocomposites.

As could be expected, intensity of TiO_2 peaks decreases with the increasing RGO content in the hybrid materials. In addition, the width of the TiO_2 peaks in T/G nanocomposites (prepared via sol-gel method) greatly increases, on one hand, compared to bare TiO_2 and, on the other hand, with the RGO content, in contrast to T/GS nanocomposites prepared by hydrothermal route which resulted more crystalline. Thus, the average crystallite sizes for T/G composites were about 9 nm, lower than those found for T/GS composites (in the range3040nm). Remarkably, in the case of T/GS-10 composite, the rutile diffraction peaks become more intense, changing the anatase: rutile ratio found in the TiO_2 bare precursor, while the other samples of this series maintained this anatase: rutile ratio (Fig. 2 and Table 1).The behavior of T/GS-10 may be explained as formation and growth of rutile crystals during hydrothermal aging (in acidic medium), which proceeded at the expenses of anatase crystals, possibly via a dissolution-precipitation mechanism [37] or by condensation of the anatase nanoparticles where, during the growth of small anatase particles by ripening, a join of their (112) facets is produced. However, this explanation does not account for the different behavior observed in the rest of samples of this series (T/GS-5, and T/GS-20) and, to this moment, we do not have a clear explanation for this feature. As previously pointed out, the crystallinities are well correlated to the specific surface areas in both series of nanocomposites. Moreover, it is noticeable that both rutile and anatase phases are present in the highly crystallized T/GS samples exhibiting the lower specific surface areas, while only anatase phase is present in the T/G series with higher specific surface areas.

Neither the characteristic peaks of GO nor of reduced graphene oxide were found in any of the composite XRD patterns, which demonstrate the reduction of GO during hydrothermal treatment produced by the loss of its oxidation debris. The results demonstrate a clear

influence of the preparation method and of the TiO_2/RGO weight ratio on the structural features of the prepared nanocomposites.

2.3. Raman measurement

Raman spectra (λ=514 nm) of samples T/GS-10 (prepared via hydrothermal route) and T/G10 (prepared by sol-gel method) as representative ones are shown in Fig. 3. Five points were measured in each sample to identify any heterogeneity of the nanocomposite material. All the prepared samples presented two characteristic bands at ca. 1350 cm^{-1} (D band) and 1604 cm^{-1} (G band) typically assigned to structural defects and to the first order scattering of the E_{2g} mode observed for sp2 carbon domains, respectively [38,39]. Thus, the intensity ratio I_D/I_G of the D and G bands is a measure widely used to quantify disorder and defect quantity in graphitic materials. The intensity ratio I_D/I_G (0.88 and 0.94) for T/G-10 and T/GS-10 nanocomposites resulted larger than that of GO (I_D/I_G =0.83) indicating an increase of graphene structural disorder upon TiO_2 incorporation and RGO reduction (Table S1). Bands corresponding to anatase phase are present in TiO_2 at around 142 ($E_g(1)$), 397 ($B_{1g}(1)$), 637 ($E_g(3)$), and 516 ($A_{1g} + B_{1g}(2)$), as well as in the T/GS-10 and T/G-10 nanocomposites, which indicates that TiO_2 nanoparticles in the composites presented a certain long-range order crystallinity. As expected, the relative intensity of the anatase bands decreased in the TiO_2/RGO nanocomposites compared to bulk TiO_2. However, the bands intensity appeared much less intense in sample T/G-10 (prepared by sol-gel) in comparison with sample T/GS10 (prepared via hydrothermal route) despite their similar RGO content, ca. 12 and 9 wt.%, respectively (Table 1). Besides, the most intense Raman mode of as-synthesized TiO_2 at 142 cm^{-1} ($E_g(1)$) blue shifted in the synthesized T/G-10 and T/GS-10 nanocomposites by about 38 cm^{-1}, as detailed in Table 2. This shift of the E_g Raman mode and the increasing peak width has been attributed to a smaller particle size in sample T/G-10 as could be confirmed by TEM and HRTEM analysis.

12

2.4. TEM and HRTEM analysis

The prepared nanocomposites and TiO$_2$ nanoparticles were studied by both TEM and

HRTEM analysis. Fig. 4 shows a general view of samples T/G-10 and T/GS-10. The TiO$_2$

particles are easily identified due to the higher electron contrast. The samples T/G-10 presents

well dispersed TiO$_2$ nanoparticles on the RGO surface, while sample T/GS-10 presents a

more heterogeneous structure with larger and agglomerated TiO$_2$ particles. Fig. 5 displays the

structural characteristics of the samples studies by HRTEM. Fig. 5A and B show lattice fringe

image along with Fourier Transform (FT) images of selected area. In T/G-10 (Fig. 5A), a

single crystallite of anatase is embedded in graphene oxide. The anatase crystallite is

identified by the spots at 2.43 Å and 2.38 Å in the FT image which correspond to the (103)

and (004) crystallographic planes. Interestingly, there is an apparent ordered growth between

TiO$_2$ and graphene oxide. This is exemplified by the alignment of the (002) graphene oxide

planes and (004) TiO$_2$ crystallographic planes. This ordering is evident in Fig. 5B, where

graphene oxide layers clearly adapt to the surface of anatase particles. In the FT, spots at 3.52

Å correspond to the (101) planes of anatase and the ring at about 3.70 Å corresponds to the

(002) planes of graphene oxide structure. This is indicative of a direct growth of anatase over

graphene oxide resulting in a strongly intermixed material, where an intimate contact between

TiO$_2$ and GO structures occurs when the nanocomposite is prepared by the sol-gel method.

On the other hand, sample T/GS-10 (prepared by hydrothermal route) is constituted by TiO$_2$

particles considerably larger than in previous sample T/G-10. These TiO$_2$ particles show

welldefined crystallographic facets, then present high crystallinity with sizes of about 30-50

nm compared to ~20 nm for T/G-10, as shown in Fig. 4B and D. Moreover, the dispersion of

TiO$_2$ over graphene oxide is lower with less intimate contact between these two components

in T/GS-10 than in sample T/G-10 (prepared by direct sol-gel method). Fig. 5C indeed shows

a representative HRTEM image, where though being in contact, no apparent structural

relationship exists between TiO_2 crystallites and graphene oxide. Spots at 2.38 and 1.70 Å correspond to the (004) and (105) crystallographic planes of anatase phase, whereas that at about 3.80 Å corresponds to RGO.

TEM micrographies of both series of samples with increasing RGO content followed the same trend, with small TiO_2 nanoparticles dispersed on the RGO surface in case of T/G series and larger TiO_2 particles with a more heterogeneous distribution in case of T/GS series. These (HR) TEM results further prove that the preparation method affects significantly the structure of the nanocomposites, as has been previously found by PXRD, Raman and N_2 adsorptiondesorption measurements.

2.5. XPS analysis

XPS of the TiO_2-RGO samples presented the typical peaks of C1s (of RGO), Ti2p (of TiO_2) and O1s of both GO and TiO_2.Notably, the surface C/Ti value was particularly high taking into account the low carbon content in the bulk observed by TGA and EDX, indicating a very high RGO dispersion. Further, the surface C/Ti ratio was slightly higher in sample T/G-10 than in T/GS-10, suggesting that TiO_2 nanoparticles in the former allowed a better dispersion of the RGO sheets on the TiO_2 matrix. The spectra in the C1s XPS region were different between samples prepared by sol-gel method and the hydrothermal route. Thereby, graphene oxide appeared clearly more reduced in sample T/G-10 than in T/GS-10 as seen from the contributions of bands at higher binding energies, more intense in sample T/GS-10 (Fig. 6A and B). This clearly indicates that the surface characteristics of both samples are different, that is, that the preparation method induces differences in the surfaces of the final materials. Similarly, the O1s XPS spectra also showed differences between samples T/G-10 and T/GS10 (Fig. 6C and D). In sample T/G-10, the O1s spectra showed two intense bands. The one at lower binding energy (at about 530 eV) is ascribed to lattice oxygen in TiO_2, whereas the band at higher binding energy, ca. 532.5 eV, is ascribed to surface oxygen groups, such as

hydroxyl. In contrast, the band at higher binding energy in the O1s spectra of sample T/GS-10 is very weak compared to the lattice oxygen band. Moreover, this band presented a shift of ca. +0.3 eV in sample T/G-10 compared to T/GS-10, suggesting a different oxygen environment. Although no direct evidence of bond between TiO_2 and RGO was found, HRTEM revealed that samples prepared by sol-gel (in this case T/G-10) consisted of a strongly intermixed material with evident order between both components. Hence, this shift could be tentatively attributed to the interaction between surface GO's oxygens and TiO_2 during hydrolysis and condensation, where oxygens belonging to GO would have contributed to the growth and nucleation of the TiO_2 nanoparticles.

Zhang et al. [20] reported that connection between TiO_2 and graphene can be assessed by studying by FTIR the adsorption band below 1000 cm^{-1} corresponding to the different Ti-OTi bonds. They observed a shift to higher wavenumbers in the TiO_2 band upon the incorporation of graphene, which they attributed to a combination of Ti-O and Ti-C bonds. Similarly to Zhang et al., T/G-10 and T/GS-10 nanocomposites presented a shift of the FTIR bands toward higher wavenumbers compared to bare TiO_2; however, more notable was the broadening suffered by these bands upon the addition of RGO and the resolution of new bands between 600 and 400 cm^{-1} (Fig. S2). This fact suggests an interaction between TiO_2 and RGO in the nanocomposite through the formation of Ti-C/Ti-O-C bonds.

2.6. Solid state UV-Vis absorbance

The determination of band gap of bare TiO_2, T/G (sol-gel method) and T/GS (hydrothermal route) materials series was performed by DRS UV-Vis absorption (Fig. S2). As an example, spectra of TiO_2, T/G-10 and T/GS-10 materials are shown in Figure 7, where a significant redshift in the maximum adsorption edge (from 355 nm to 378 nm) is observed upon the addition of RGO leading to small energy band gap narrowing. The obtained results were converted and assuming indirect transition to obtain the band gap values: 3.26 eV for

prepared TiO_2 nanoparticles shifting to 3.10 eV when mixed with RGO in the composites. This band gap reduction is known to be produced by interaction between C and Ti atoms which reduces the recombination of photo-generated electron-hole pairs [15].

3. Photocatalytic test

The photocatalytic performance of T/G and T/GS nanocomposites was measured by degradation of MB as model contaminant under UV light irradiation (365 nm). Fig. 8, presents a plot of C/C_0 versus irradiation time, where C_0 is the initial concentration and C the concentration at different time of MB. Bare TiO_2 was used as reference under the same conditions. During the photocatalytic process, photocatalysts are excited and the photogenerated electrons can be transferred to the nearby MB and participate to the redox reactions, leading to the decomposition of MB into CO_2 and H_2O [40]. The normalized temporal concentration changes (C/C_0) of MB during the reaction were calculated by measuring the absorbance of MB in each aliquot at 664 nm at a given time interval. The blank test of MB degradation (i.e. without catalyst) indicated that photolysis was negligible. Adsorption of MB in dark conditions was performed during 60 min before photocatalysis. The samples of TG series reached higher adsorption capacity than the samples of T/GS series with maximum adsorptions of 43% and 35%, respectively (Table 2), essentially due to higher porosity and specific surface area presented by T/G samples (Table 1). Moreover, adsorption increased with the increasing RGO content, as could be expected. After dark test, the MB was submitted to UV radiation up to 240 min for photo-degradation studies (Fig. 8(A) and 8(B)). Bare TiO_2 showed less activity than the nanocomposites, because of the well-known rapid recombination effect of photo-generated electron-hole pairs [41]. The incorporation of RGO in TiO_2 allowed an enhancement in photocatalytic degradation compared to bare TiO_2 mainly due to the lower recombination rate of photo-generated electrons and holes in the

16

nanocomposites. Moreover, adsorption of MB on the reduced graphene oxide also resulted beneficial to the photocatalytic activity [42].

The efficiency of the photocatalysts was observed being dependent on the TiO_2/RGO ratio, with an optimal RGO loading of ca. 10 wt.% in both series of photocatalysts (T/G-10 and T/GS-10) with 93% and 82% of MB removal, respectively (Table 2). Higher RGO loadings in the nanocomposites resulted in a marked decrease in the MB removal. Despite higher RGO loadings favor MB adsorption; the decrease in the MB removal at higher RGO contents may account for a lower access of the photoactive TiO_2 sites. Furthermore, the degradation of MB was greater over the T/G series of photocatalysts (i.e, prepared by sol-gel) than on the T/GS photocatalysts (prepared via hydrothermal route) showing that the different surface and structural features of both series of nanocomposites, due to the different preparation route, have a great effect on their photocatalytic activity. Hence, the higher surface area of T/G photocatalysts which improved MB adsorption on their surface, thus favoring photodegradation; the smaller particle size and enhanced dispersion of the TiO_2 nanoparticles; as well as the RGO-TiO_2 peculiar interaction account for the greater photodegradation observed in the T/G series.

The photocatalytic degradation with the other results from the literature is compared in Table S6 [21,23,43-46]. The comparison with different samples is based on composition, pollutant, source of irradiation, time and photocatalytic degradation. It was observed the photocatalytic activity with the same materials as this work (TiO_2/RGO) depends on the experimental conditions. The best performances has been reported with TiO_2/RGO prepared by solvothermal method for the degradation of Rhodamine B, obtaining a $C/C_0 = 0.05$ under visible light irradiation, but after 5 h [23]. Degradation of MB by TiO_2/RGO nanorods presented $C/C_0 = 0.18$ under visible light, in the same range than sample T/GS-10 after 100 min [43]. However, the photocatalytic activity of Ag-CNT/TiO_2 catalysts for degradation of

acid orange 7 under visible light was $C/C_0 = 0.25$ after 1 h [44]. The T/G-10 and T/GS-10

samples showed degradations of $C/C_0 = 0.18$ and 0.07 after 3 h which are comparable (and

better in some cases) with other reported materials based on TiO_2/RGO.

Catalysts $CNT/P\text{-}TiO_2$ prepared by hydrothermal method for methyl orange degradation under

visible UV light (250W, 420 nm) presented total degradation [21]. However, catalysts

TiO_2/CB [45] and $CNT/Fe\text{-}Ni/TiO_2$ [46] presented degradations of $C/C_0 = 0.12$ (MO) and 0.10

(MB), respectively.

From literature, it is noticeable that photodegradation is dependent on the type of material,

dye and conditions used (i.e., irradiation source, concentrations, etc). However, the results

reported up to date, presented degradation values comparable to those found for our

synthesized materials T/G-10 and T/GS-10, prepared via simple methods and without the

addition of noble metals. Thus, these samples could be promising in the photocatalysis field.

Further, we have compared (in identical operational conditions) that the preparation method

has a great influence on the final properties of the materials.

The effect of the mass of photocatalyst on the MB removal was also studied (SI). The mass of

nanocomposites T/G-10 and T/GS-10 was varied from 50 mg to 125 mg and the MB

concentration was maintained at 10 mg/L in all the experiments. As expected, an increment in

mass of photocatalyst led to the increase of both the adsorption and photocatalytic

degradation. Again, catalyst T/G-10 showed better performance than its analogous T/GS-10

in all the range of mass concentration studied, and complete MB removal was observed after

240 min with catalyst loading of 125 mg.

The effect of methylene blue concentration on the photocatalytic degradation of T/G-10 and

T/GS-10 under UV light irradiation was studied by varying its concentration between 5 mg/L

and 12.5 mg/L (SI). The concentration of photocatalyst was fixed at 500 mg/L. As expected,

MB adsorption increased with the increasing initial concentration in both photocatalysts.

Notably, catalyst T/G-10 showed complete MB removal at the lower initial concentrations (i.e., 5 and 7.5 mg/L). Further, for an initial MB concentration of 5 mg/L, complete removal was observed in 90 min compared to 240 min needed for catalyst T/GS-10 for the same initial concentration of MB. The MB removal decreased with the increasing initial concentration, the photocatalyst T/G-10 presenting a 71% of MB removal after 240 min of UV exposition at the highest MB concentration tested (12.5 mg/L) compared to 61% showed by T/GS-10 photocatalyst.

The influence of the initial MB concentration on the photocatalytic removal rate was studied following the Langmuir-Hinshelwood model (eq. 2) and reducing the expression to a firstorder kinetic expressed by the equation 3.

$$r = -dC/dt = k_r K C / (1 + KC) \tag{2}$$

$$ln\, C/C_0 = K_{ap}\, t \tag{3}$$

Where K_{ap} (min^{-1}) is the apparent rate constant of the first-order reaction, C is the concentration of MB at a reaction time (t) and C_0 is the equilibrium concentration of MB after adsorption in dark conditions. The kinetic plots for photocatalytic removal of MB are presented in SI in Fig. S7. Table 2 shows the photodegradation evolved for all the nanocomposites, where T/G-10 and T/GS-10 present the highest rates of MB removal, that of the former being more than two times that of the later ($1.12 \cdot 10^{-2}$ and $4.78 \cdot 10^{-3}$ min^{-1}, respectively). Indeed, despite the similar RGO content in both T/G-10 and T/GS-10 photocatalysts, T/G-10 showed superior performance in all the tests performed. This fact clearly highlights that the synthesis route followed for the preparation of the TiO$_2$-RGO nanocomposites have an important role on their surface properties, which ultimately will mirror on their photocatalytic activity.

4. Conclusions

The comparison of groups of nanocomposites prepared by following two different sol-gel and hydrothermal routes demonstrated that other parameters than the composition should be considered to account for the photocatalytic performances. In this work, we showed that TiO$_2$-RGO nanocomposites presented, in all the cases studied, improved photocatalytic properties compared to bare TiO$_2$. An optimal composition, in terms of TiO$_2$/RGO ratio was found in both series of nanocomposites; however, superior activity was found for those prepared by direct sol-gel route.

The physico-chemical characterizations of the prepared nanocomposites, revealed the different properties of both series of samples due to their preparation protocol. Thus, it was observed that nanocomposites prepared by sol-gel method presented improved textural properties than those prepared following a hydrothermal route. The preparation route also affected the structure of the nanocomposite. The sol-gel method has a clear influence not only on the mean particles size which is by far lower, but also inhibits the formation of rutile cophase. On the other hand, TEM and HRTEM microscopies revealed that the TiO$_2$ nanocrystals were more homogenously deposited on RGO in T/G samples prepared by sol-gel method. The differences of structural and textural properties of both series of samples influence their catalytic activity which is more than twofold enhanced in case of T/G series obtained by sol-gel method, especially in T/G-10 nanocomposites, compared to its analogous T/GS-10 sample obtained by hydrothermal route, both samples prepared with GO content of 10 wt.%. The T/G nanocomposites in particular also presented great adsorptivity of MB, highly important for an efficient photocatalytic activity.

The improved photocatalytic activity in the T/G series of nanocomposites can be attributed to a closer contact between TiO$_2$ nanoparticles and RGO, their better dispersion and

homogeneous distribution and the enhanced textural properties which certainly influence on their adsorptive properties and photoresponse range.

In summary, we have proved that optimization in the preparation of hybrid photocatalysts is needed to obtain materials with finer properties for effective application in environmental issues.

Acknowledgements

References

[1] N. Savage, M.S. Diallo, J. Nanopart. Res. 7 (2005) 331-342

[2] A.M. Dutta, S.K. Maji, B. Adhikary, Mat. Res. Bull. 49 (2014) 28-34

[3] N.M. Mahmoodi, Mat. Res. Bull. 48 (2013) 4255-4260

[4] N. Wang, J. Xu, L. Guan, Mat. Res. Bull. 46 (2011) 1372-1376

[5] S.D. Dalt, A.K. Alves, C.P. Bergmann, Mat. Res. Bull. 48 (2013) 1845-1850

[6] D. Sánchez-Martínez, A. Martínez-de la Cruz, E. López-Cuéllar, Mat. Res. Bull. 48 (2013) 691-697

[7] Y. Lin, C. Ferronato, N. Deng, J.-M. Chovelon, Appl. Catal. B Environ. 104 (2011) 353-360.

[8] A. Molea, V. Popescu, N.A. Rowson, Powder Technol. 230 (2012) 203-211.

[9] X.-L. Peng, M.-M. Yao, F. Li, X.-H. Sun, Part. Sci. Technol. 30 (2012) 81-91. [10] A. Molea, V. Popescu , N.A. Rowson , A.M. Dinescu, Powder Technol. 253 (2014) 22-28.

[11] X. Zhang, Y. Wang, B. Liu, Y. Sang, H. Liu, Appl. Cat. B : Environ. 202 (2017) 620-641

[12] J. Tian, Z. Zhao, A. Kumar, R.I. Boughton, H. Liu, Chem. Soc. Rev. 43 (2014) 69206937

[13] J. Tian, Y. Leng, Z. Zhao, Y. Xia, Y. Sang, P. Hao, J. Zhan, M. Li, H. Liu, Nano Energy, 11 (2015) 419-427

[14] J. Tian, X. Hu, N. Wei, Y. Zhou, X. Xu, H. Cui, H. Liu, Sol. Energy. Mat. Sol. Cells. 151 (2016) 7-13

[15] X. Zhang , Y. Sun, X. Cui , Z. Jiang, Internat. J. of Hydrogen Energy. 37 (2012) 811-815.

[16] S. Fukahori, H. Ichiura, T. Kitaoka, H. Tnaka, Environ. Sci. Tech. 37 (2003) 1048-1051.

[17] J. Aguado, R. Van Grieken, M.J. Lopez-Munos, J. Marugan, J. Appl. Catal. A. 312 (2006) 202-212.

[18] J. Matos, A. Garcia, T. Cordero, J.M. Chovelon, C. Ferronato, Catal. Lett. 130 (2009) 568-574.

[19] D. Wang, D. Choi, J. Li, Z. Yang, Z. Nie, R. kou, D. Hu, C. Wang, L.V. Saraf, J. Zhang, I. A. Aksay, J. Liu, ACS Nano. 3 (2009) 907-914.

[20] H. Zhang, X. Lv, Y. Li, Y. Wang, J. Li, ACS Nano. 4 (2009) 380-386.

[21] S. Wang, S. Zhou, J. Hazard. Mater. 185 (2011) 77-85.

[22] M.J. Allen, V.C. Tung, R.B. Kaner, Chem. Rev. 110 (2010) 132-145.

[23] D. Maruthamani, D. Divakar, M. Kumaravel, J. Ind. and Eng. Chem. 30 (2015) 33-43.

[24] D.M. Chen, Q. Zhu, Z.J. Lv, X.T. Deng, F.S. Zhou, Y.X. Deng, Mat. Res. Bull. 47 (2012) 3129-3134.

[25] M.X. Sun, X.Y. Zhang, J. Li, X.L. Cui, D.L. Sun, Y.H. Lin, Electrochem. Commun. 16 (2012) 26-29.

[26] Y. H. Ng, I. V. Lightcap, K. Goodwin, M. Matsumura and P. V. Kamat, J. Phys. Chem. Lett.1 (15) (2010) 2222-2227

[27] W.S. Wang, D.H. Wang, W.G. Qu, L.Q. Lu, A.W. Xu, J. Phys. Chem. C 116 (2012) 19893-19901.

[28] M. Aleksandrzak, P. Adamski, W. Kukułka, B. Zielinska, E. M. West, Appl. Surf. Sci. 331 (2015) 193-199.

[29] T.D. Nguyen-Phan, V.H. Pham, E.W. Shin, H.D. Pham, S. Kim, J.S. Chung, E.J. Kim, S.H. Hur, Chem. Eng. J. 170 (2011) 226-232.

[30] B. Neppolian, A. Bruno, C.L. Bianchi, M. Ashokkumar, Ultrason. Sonochem. 19 (2012) 9-15.

[31] G.D. Jiang, Z.F. Lin, C. Chen, L.H. Zhu, Q. Chang, N. Wang, W. Wei, H.Q. Tang, Carbon. 49 (2011) 2693-2701.

[32] D.L. Zhao, G.D. Sheng, C.L. Chen, X.K. Wang, Appl. Catal. B 111-112 (2012) 303-308.

[33] C. Chen, W.M. Cai, M.C. Long, B.X. Zhou, Y.H. Wu, D.Y. Wu, Y.J. Feng, ACS Nano. 4 (2010) 6425-6432.

[34] W.S. Hummers Jr., R.E. Offeman, J. Am. Chem. Soc., 1958, 80 (6), 1339-1339. [35] C. Wang, M. Cao, P. Wang, Y. huiAo, J. Hou, J. Qian, , Appl. Cata. A: General 473 (2014) 83-89.

[36] X. Zhang, H. Li, X. Cui, Y. Lin, J. Mater. Chem. 20 (2010) 2801-2806.

[37] M. Kondo, K. Shinozaki, R. Ooki, N. Mizutani,J. Ceram. Soc. Jpn. 102 (1994) 742-746.

[38] A.C. Ferrari, Solid state commun. 143 (2007) 47-57.

[39] M.A. Pimenta, G. Dresselhaus, L.G. Cançado, A. Jorio, R. Saito. Phys. Chem. Chem. Phys. 9 (2007) 1276-1290.

[40] L.C.A. Oliveira, C.V.Z. Coura, I.R. Guimaraes, M.G. Alves, J. Hazard. Mater. 192 (2011) 1094-1099.

[41] D. Liang, C. Cui, H. Hu, Y. Wang, S. Xu, B. Ying, P. Li, B. Lu, H. Shen, J. Alloys

Compd. 582 (2014) 236-240.

[42] X. Wang, R.A. Caruso, J. Mater. Chem. 21 (2011) 20-28.

[43] M. Sun, W. Li, S. Sun, J. He, Q. Zhang, Y. Shi, Mat. Res. Bull. 61 (2014) 280-286.

[44] Z. Feng-jun, C. Ming-liang, O. Won-chun, New Carbon Mater. 25(5) (2010) 348-356.

[45] C. Mao, H. Weng, Chem. Eng. J. 155 (2009) 744-749.

[46] L. Ma, A. Chen, J. Lu, Z. Zhang, H. He, C. Li, Particuology 14 (2014) 24-32.

Figures Caption

Fig. 1. Nitrogen adsorption-desorption isotherms of TiO_2 and RGO (A), T/G samples (B), and T/GS samples (C)

Fig. 2. PXRD patterns of the different catalysts: (A) T/G samples (B) T/GS samples.

Fig. 3. Raman spectra of samples GO, T/G-10, T/GS-10 and TiO_2 (inset).

Fig. 4. TEM images of A, B) T/G-10 (prepared by direct sol-gel method) and C, D) T/GS-10 (prepared by hydrothermal method).

Fig. 5. HRTEM images of A, B) T/G-10 and C) T/GS-10.

Fig. 6. C1s core-level spectra of A) T/G-10 and B) T/GS-10 patterns, and O1s core-level spectra of C) T/G-10 and D) T/GS-10 patterns.

Fig. 7. Diffuse reflectance absorption spectra of TiO_2, T/G-10 and T/GS-10.

Fig. 8. Photocatalytic degradation efficiency of methylene blue of: (A) T/G samples and (B) T/GS samples. Experimental conditions: UV light irradiation (λ=365 nm), MB concentration (10 mg/L), mass of the catalyst (100 mg), MB volume (200 mL).
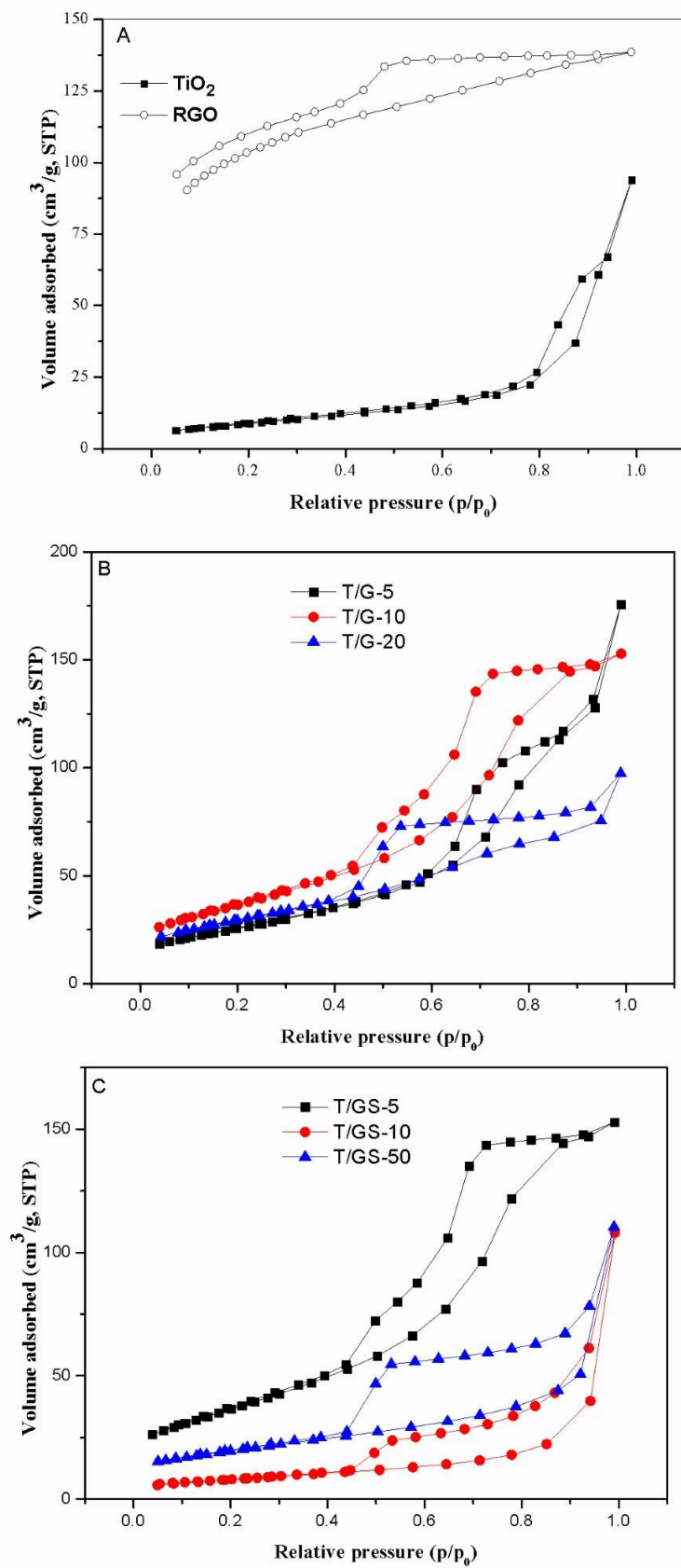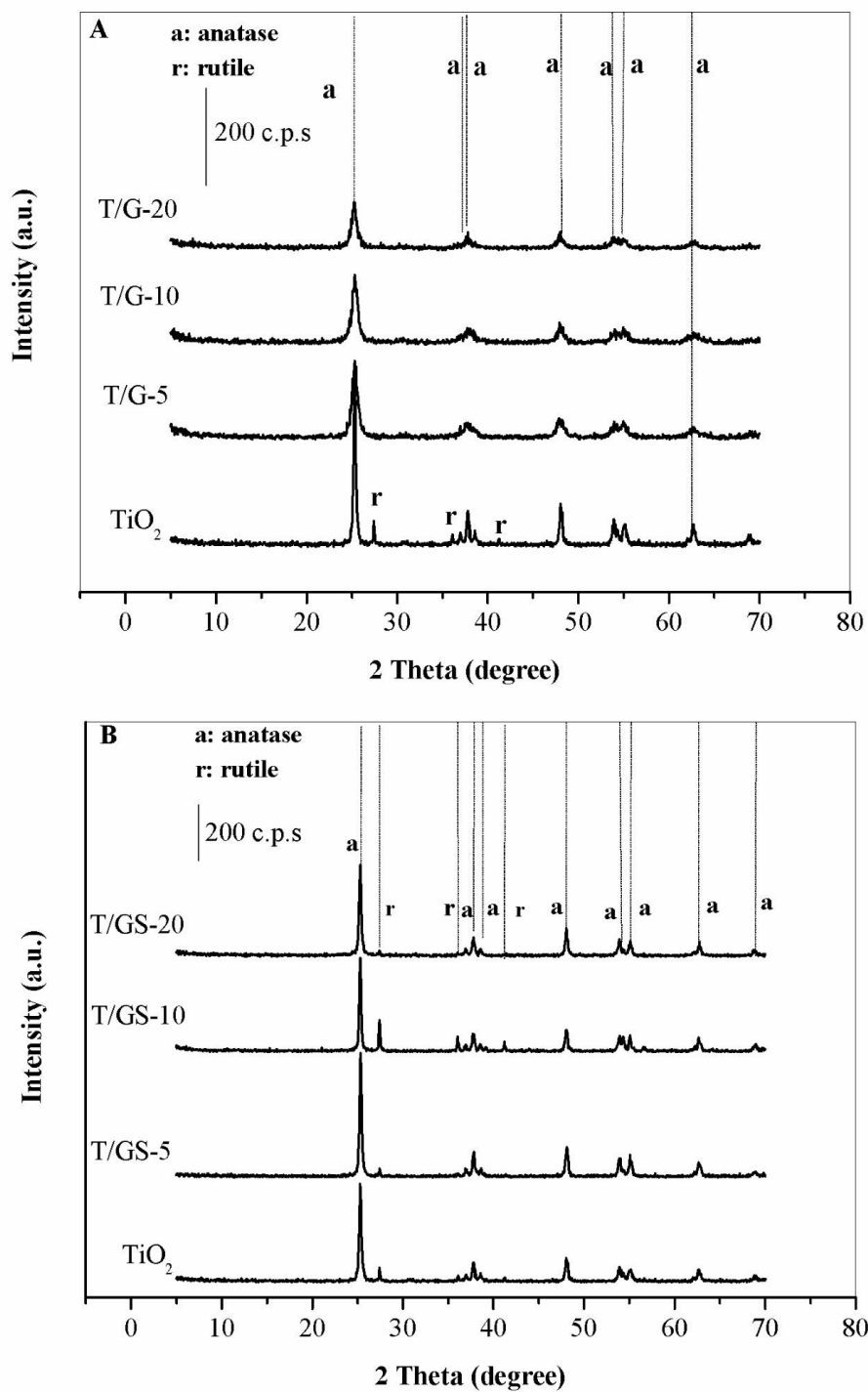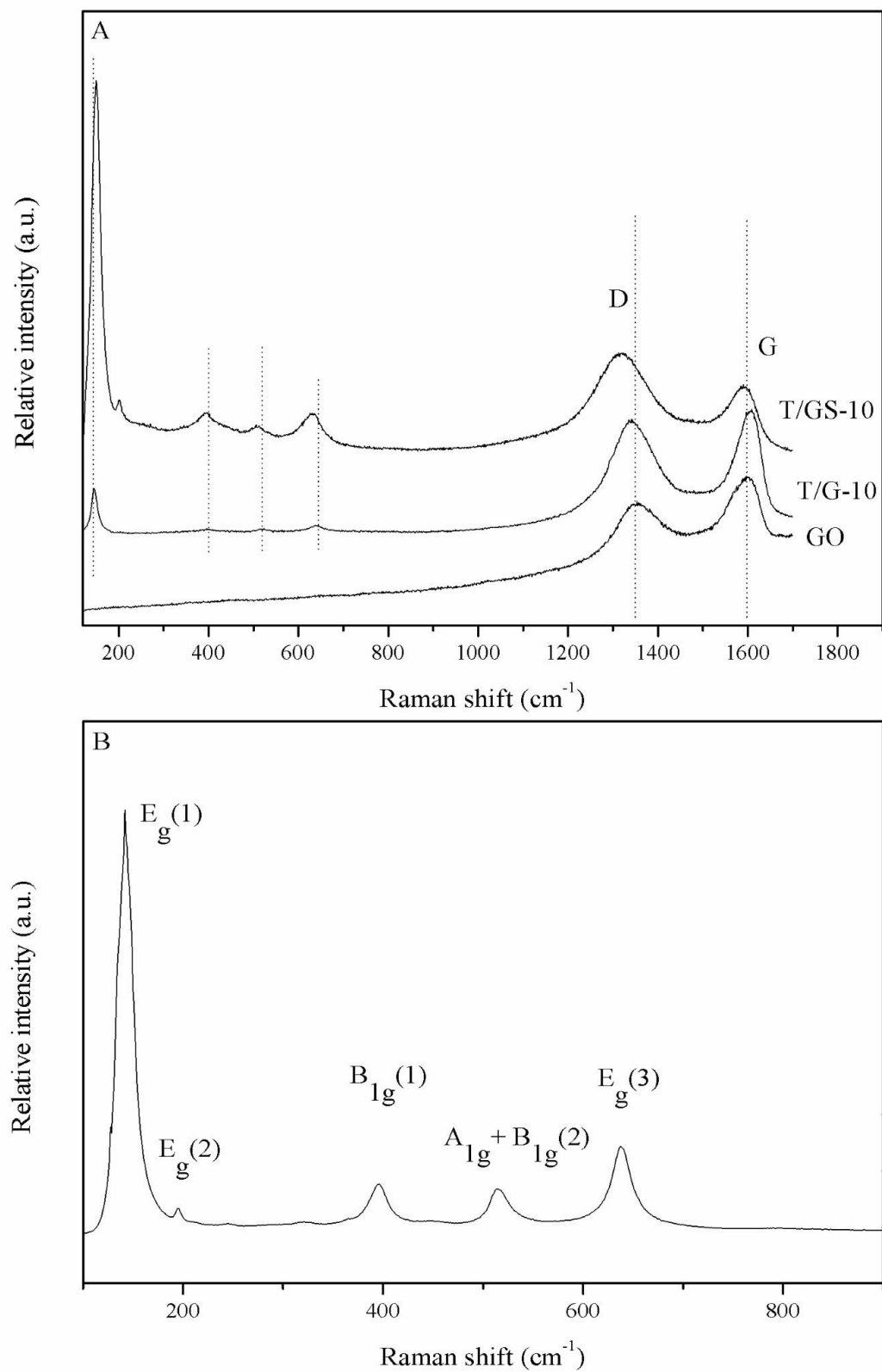
Fig. 1. Nitrogen adsorption-desorption isotherms of TiO$_2$ and RGO (A), T/G samples (B), and T/GS samples (C)

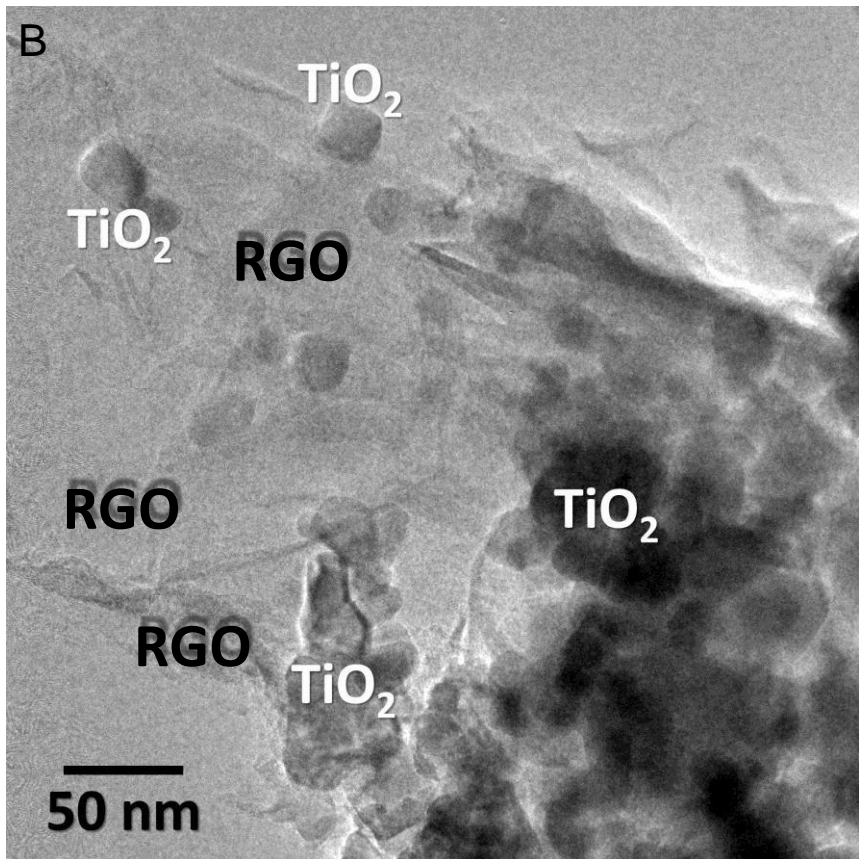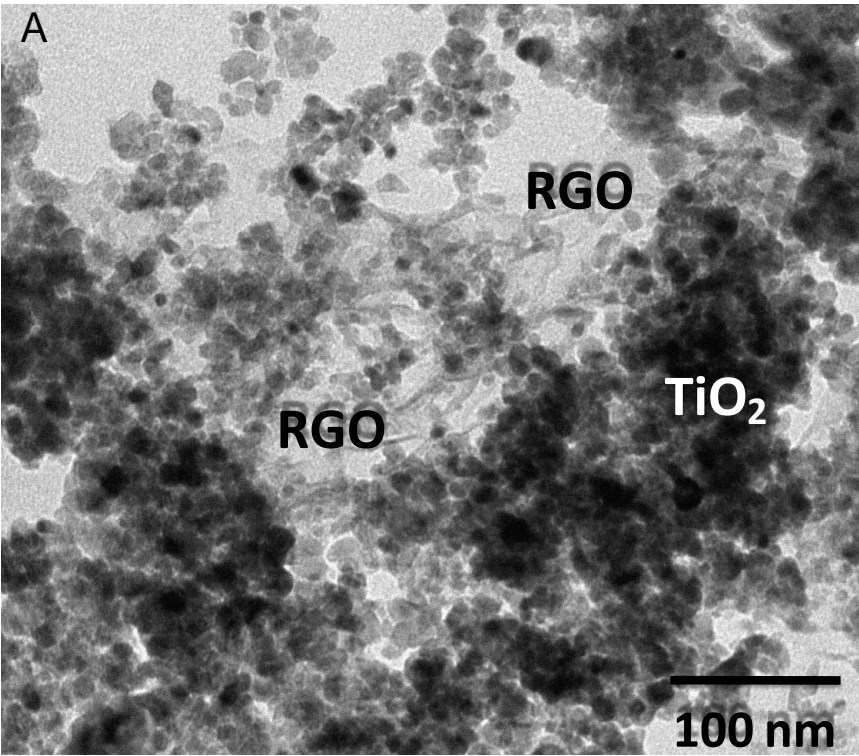**Fig. 2.** PXRD patterns of the different catalysts: (A) T/G samples (B) T/GS samples.

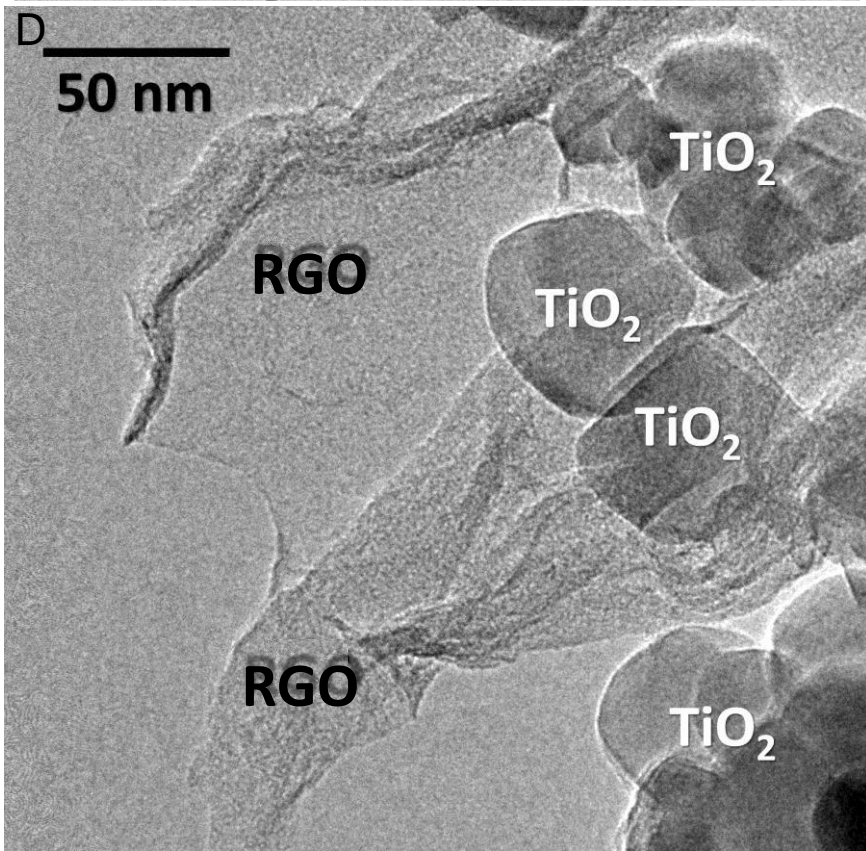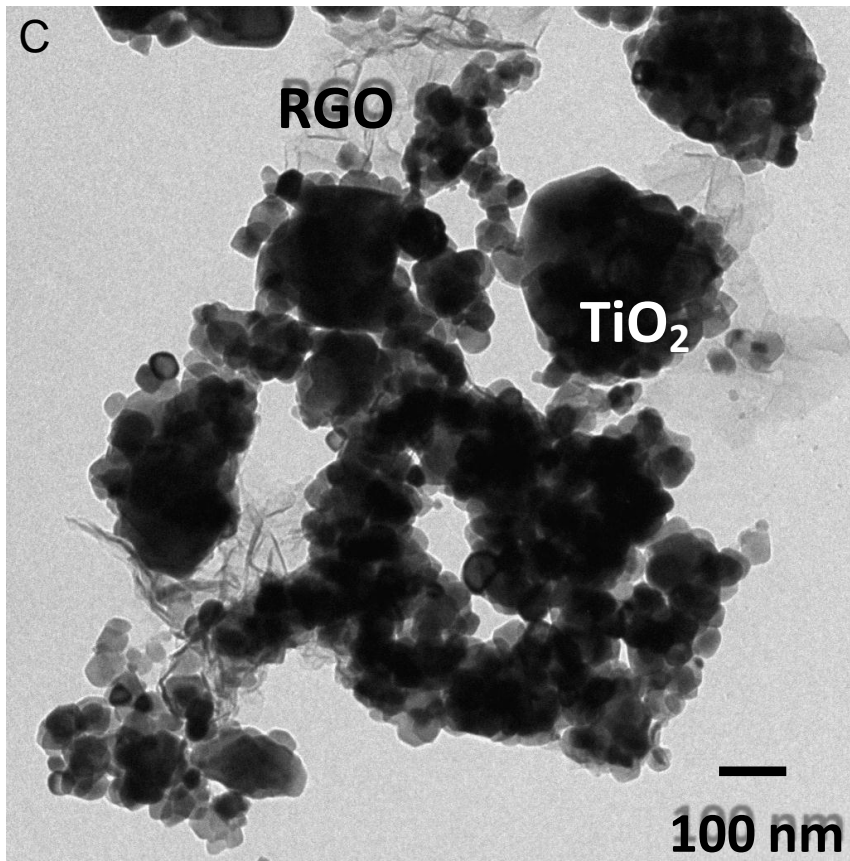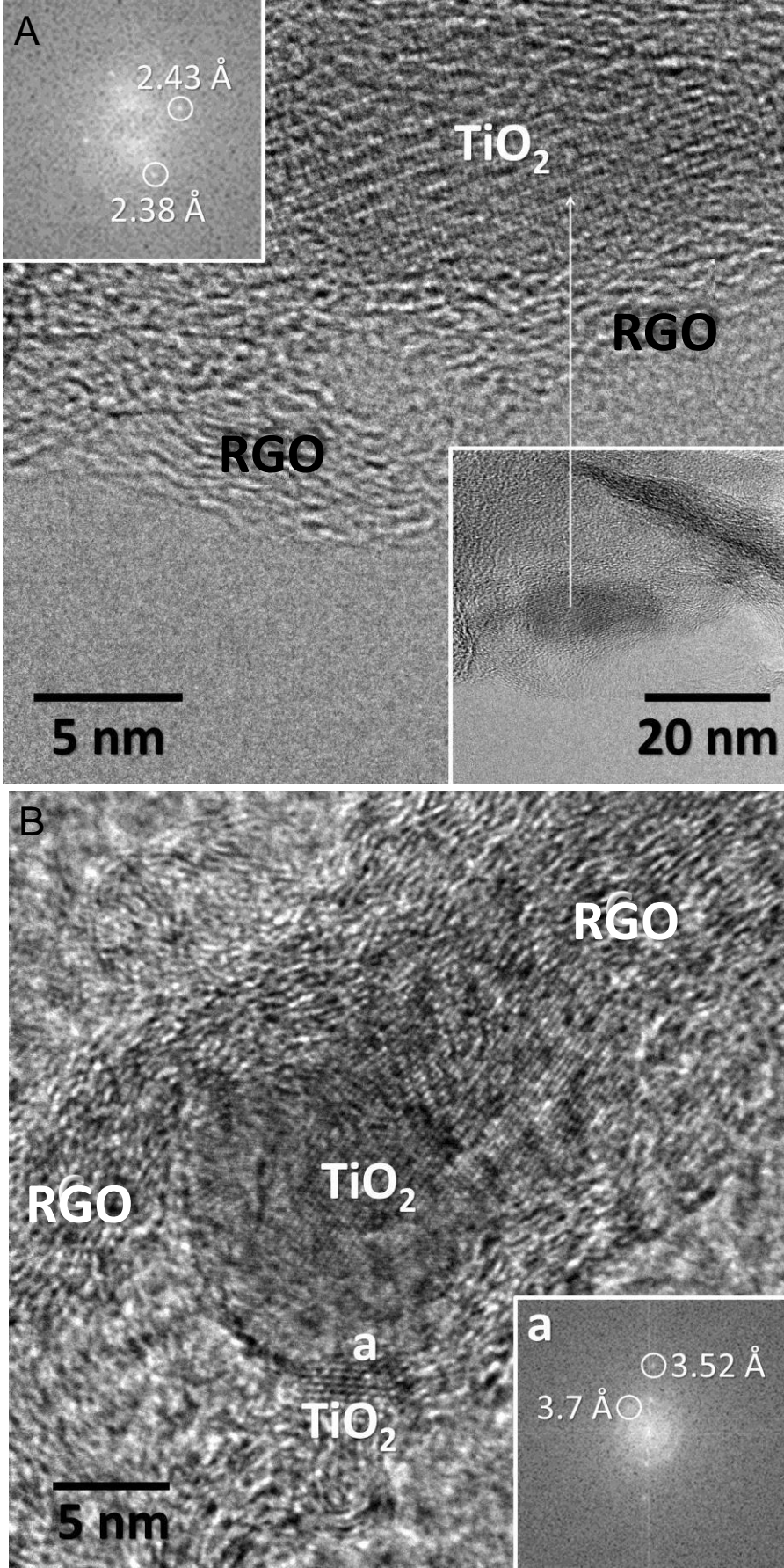**Fig. 3.** Raman spectra of: A) samples GO, T/G-10, T/GS-10 and B) TiO_2.

Fig. 4. TEM images of A, B) T/G-10 (prepared by direct sol-gel method) and C,D) T/GS-10
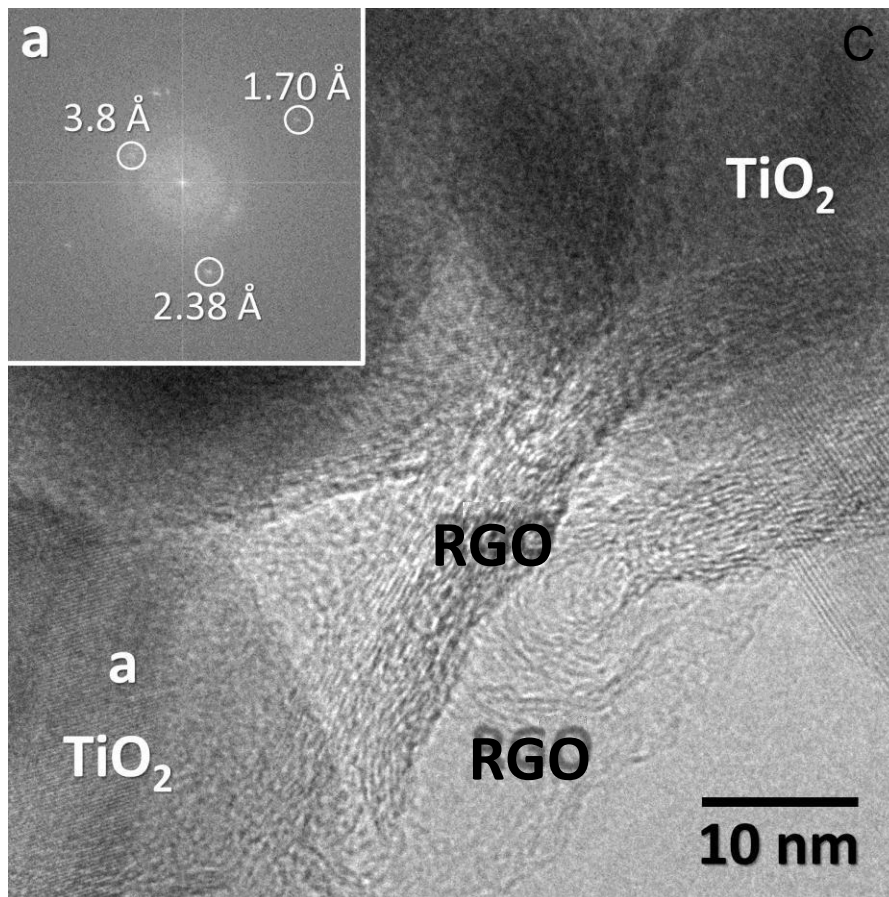
(prepared by hydrothermal method).
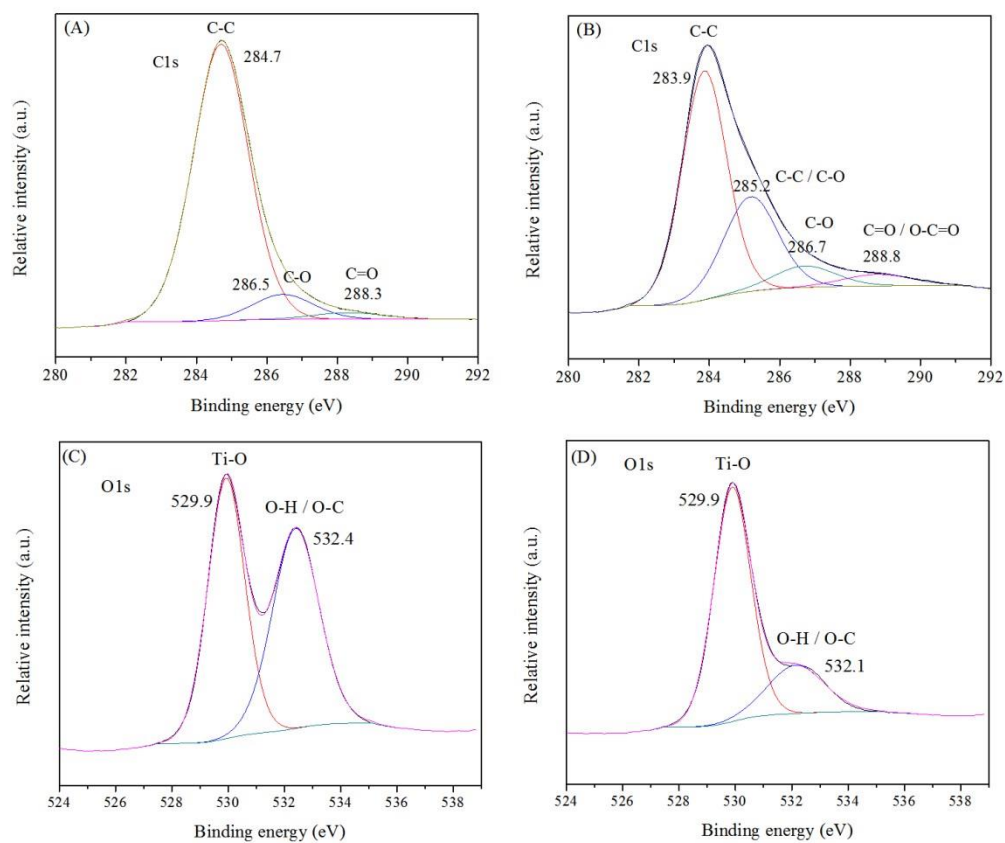
Fig. 5. HRTEM images of A, B) T/G-10 and C) T/GS-10.

Fig. 6. C1s core-level spectra of A) T/G-10 and B) T/GS-10 patterns, and O1s core-level spectra of C) T/G-10 and D) T/GS-10 patterns.

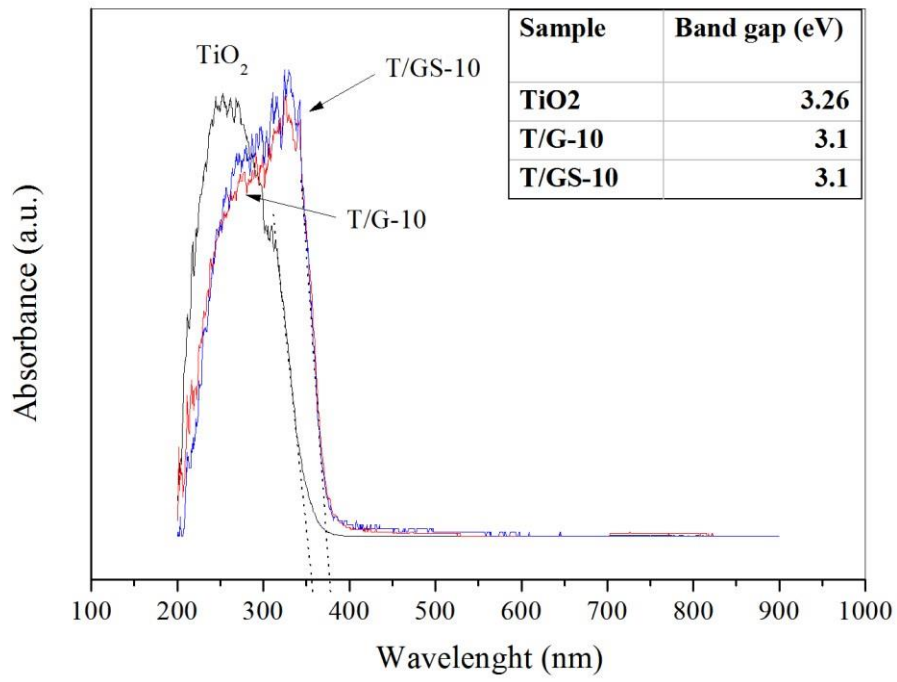| Sample	Band gap (eV)
TiO2	3.26
T/G-10	3.1
T/GS-10	3.1

Fig. 7. Diffuse reflectance absorption spectra of TiO_2, T/G-10 and T/GS-10.
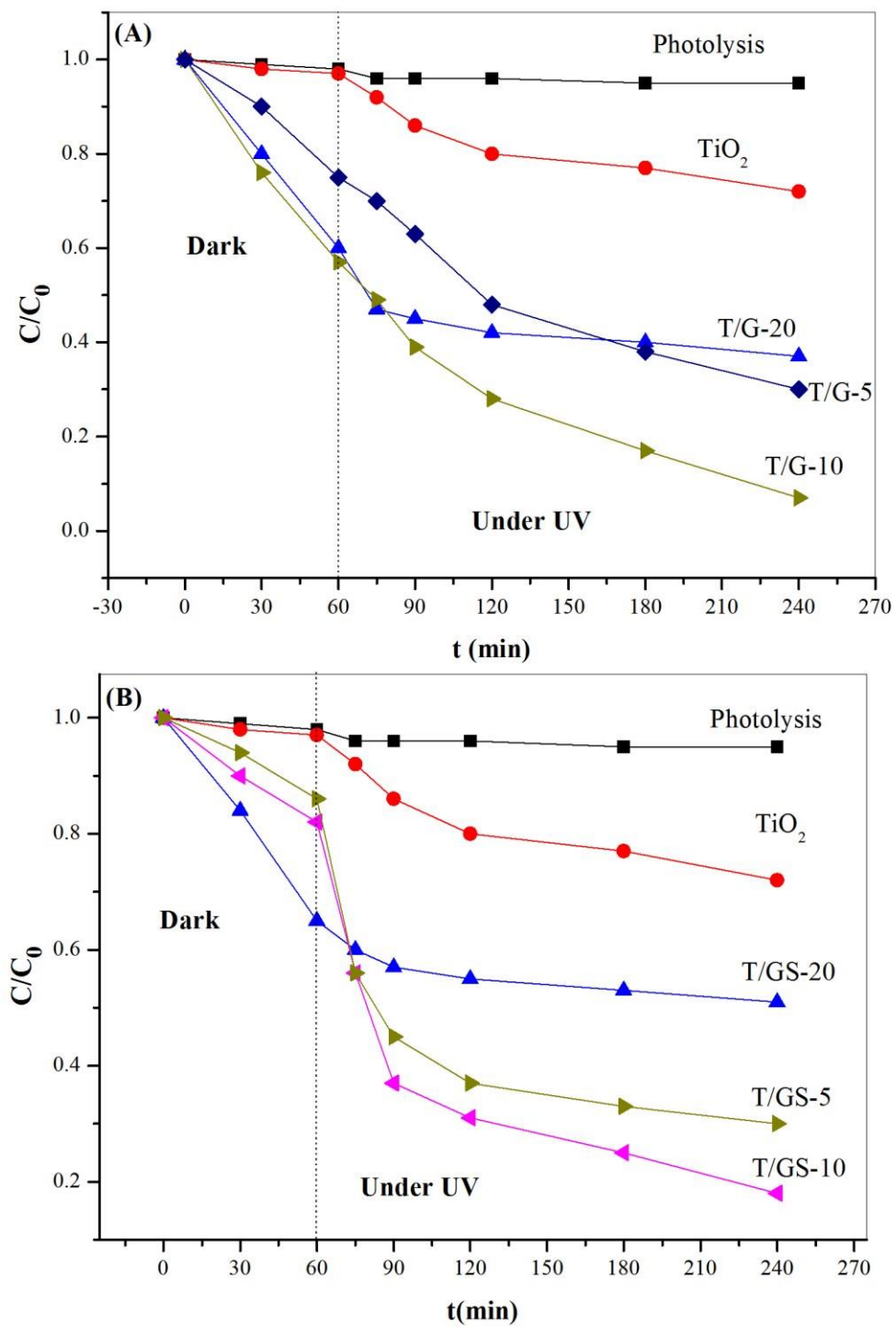
Fig. 8. Photocatalytic degradation efficiency of methylene blue of: (A) T/G samples and (B) T/GS samples. Experimental conditions: UV light irradiation (λ=365 nm), MB concentration (10 mg/L), mass of the catalyst (100 mg), MB volume (200 mL).

Table 1. Structural, chemical and textural characteristics of the different prepared samples. [a] Single-point total pore volume at $P/P_0 = 0.95$.

Sample	S_{BET} (m^{2}g^{-1})	V_P (cm^3/g)[a]	D_p (nm)[b]	Anatase content[c]	Rutile content[c]	Crystallite size (nm)[d]	RGO content (%)[e]
RGO	333.9	1.46	3.68	-	-	-	-
TiO$_2$	32.4	0.99	11.66	90.3	9.7	28.4(10)	-
T/G-5	94.0	1.85	6.43	100	-	9.01(30)	4
T/G-10	134.0	1.61	6.42	100	-	8.6(31)	12
T/G-20	105.7	1.02	3.82	100	-	9.4(40)	20
T/GS-5	18.5	0.77	3.69	n.d	n.d	n.d	4
T/GS-10	28.8	1.14	3.79	75.8	24.2	37.7(16)	9
T/GS-20	68.9	1.16	3.78	95.4	4.5	29.2(10)	19

[b] BJH desorption average pore diameter. [c] Referred only to the crystalline phase. [d] Referred to anatase phase. [e] Reduced graphene oxide content calculated by TGA.

Table 2. Results of methylene blue removal over the different materials

Sample	Adsorption (C/C$_0$)	Removal (%)	Photocatalytic degradation (C/C$_0$)	Removal (%)	Degradation rate (min^{-1})[a]
Photolysis	0.98	2	0.95	5	1.29 10^{-4}
TiO$_2$	0.97	3	0.72	18	1.53 10^{-3}
T/G-5	0.75	25	0.30	70	5.18 10^{-3}
T/G-10	0.57	43	0.07	93	1.12 10^{-2}

T/G-20	0.60	40	0.37	23	$2.04\ 10^{-3}$
T/GS-5	0.86	14	0.30	70	$4.78\ 10^{-3}$
T/GS-10	0.82	18	0.18	82	$7.27\ 10^{-3}$
T/GS-20	0.65	35	0.51	49	$1.14\ 10^{-3}$

[a] Under the following reaction conditions: UV light irradiation (λ=365 nm), MB concentration (10 mg/L), mass of the catalyst (100 mg), MB volume (200 mL).

Table 3: Surface and bulk chemical analyses.

Sample	Name	FWHM	%At Conc	C/Ti	%At conc[1]
T/G-10	C 1s O	1.928	44.9		3.5
	1s	1.774	45.5	4.7	40.6
	Ti 2p 3/2	1.431	9.6		55.9
T/GS-10	C 1s O	2.077	51.0		5.5
	1s	1.631	37.4	4.4	38.8
	Ti 2p 3/2	1.429	11.6		55.7

[a] Observed in bulk by EDX

Table 4: Results of methylene blue removal over the different materials

Sample (min$_{-1}$)a	Adsorption		Photocatalytic degradation		Degradation rate
	(C/C_0)	Removal (%)	(C/C_0)	Removal (%)	
Photolysis	0.98	2	0.95	5	$1.29\ 10^{-4}$
TiO$_2$	0.97	3	0.72	18	$1.53\ 10^{-3}$
T/G-5	0.75	25	0.30	70	$5.18\ 10^{-3}$

[1] Under the following reaction conditions: UV light irradiation (λ=365 nm), MB concentration (10 mg/L), mass of the catalyst (100 mg), MB volume (200 mL).

T/G-10	0.57	43	0.07	93	1.12×10^{-2}
T/G-20	0.60	40	0.37	23	2.04×10^{-3}
T/GS-5	0.86	14	0.30	70	4.78×10^{-3}
T/GS-10	0.82	18	0.18	82	7.27×10^{-3}
T/GS-20	0.65	35	0.51	49	1.14×10^{-3}